Computer Simulation of Quantum Phenomena in Nano-Scale Devices

HANS DE RAEDT

Institute for Theoretical Physics and Materials Science Centre
University of Groningen, Nijenborgh 4
NL-9747 AG Groningen, The Netherlands
E-mail: deraedt@phys.rug.nl

ABSTRACT

This paper reviews the general concepts for building algorithms to solve the time-dependent Schrödinger equation and to discuss ways of turning these concepts into unconditionally stable, accurate and efficient simulation algorithms. Applications to focussed electron emission from nano-scale sources, mesoscopic normal-metal–superconductor devices, and charged-particle interferometry, combining features of both the Aharonov-Bohm and Hanbury Brown-Twiss experiment illustrate the power and flexibility of the simulation method.

1. Introduction

Progress in nano-scale lithography has made it possible to perform "electron-optics" experiments in solid state devices[1,2]. In an ideal device the motion of the electrons is not affected by interactions with impurities, phonons etc., i.e. the electrons travel ballistically, just as they would do in ultra-high vacuum. In real devices, typical distances for ballistic motion can be as large as $250\lambda_F$, λ_F being the Fermi wavelength of the electrons[2]. For GaAs-heterostructures $\lambda_F \approx 300$Å.

A similar, but otherwise unrelated, break-through is the development of atom-size field-electron-emission sources. Recent experiments have demonstrated that these atom-size tips act as unusual electron beam sources, emitting electrons at fairly low applied voltages (a few thousand volts or less) with a small angular spread (of a few degrees).[3,4] These properties make such electron sources very attractive for applications to electron microscopy, holography and interferometry.[5] For the materials used to fabricate the tips, e.g. tungsten, iron, gold, ..., $\lambda_F \approx 10$Å.

From physical point of view, both these nano-scale structures have at least one important generic feature: The characteristic dimensions of these devices are comparable to the wavelength (typically the Fermi wavelength λ_F) of the relevant particles (typically electrons). Under this stringent condition, a classical, "billiard-

ball" description of the particle motion is no longer valid. A calculation of the device properties requires a full quantum-mechanical treatment.

In the remainder of this review we will discuss algorithms to simulate models for such systems. The theoretical concepts underlying the algorithms are given in Sections 2 and 3. Section 4 illustrates these concepts for the case of a simple example. An algorithm for simulating the motion of a quantum particle in an inhomogenous magnetic field is presented in Section 5. Methods of analyzing the data generated by TDSE solvers are briefly discussed in Section 6. Applications to focussed electron emmision from nano-tips (Section 7.1), to Andreev reflection in mesoscopic devices (Section 7.2), and to the Aharonov-Bohm and Hanbury-Brown Twiss experiment (Section 7.3) serve to illustrate the simulation approach. The conclusions are given in Section 8.

2. Theory

The dynamic properties of a non-relativistic quantum system is governed by the time-dependent Schrödinger equation (TDSE)

$$i\hbar \frac{\partial}{\partial t}|\Phi(t)\rangle = \mathcal{H}|\Phi(t)\rangle \quad , \tag{1}$$

where $|\Phi(t)\rangle$ represents the state of the system described by the Hamiltonian $\mathcal{H}$ (here and in the following we use $\mathcal{H}$ to denote the differential operator and H for the hermitian matrix representing $\mathcal{H}$). In analogy with ordinary differential equations, the formal solution of the matrix differential equation

$$\frac{\partial}{\partial x}U(x) = HU(x) \quad ; \quad U(0) = I \quad , \tag{2}$$

where I denotes the $M \times M$ unit matrix and H is a $M \times M$ matrix, is given by

$$U(x) = e^{xH} \quad , \tag{3}$$

and is called the exponential of the matrix H. In quantum physics and quantum statistical mechanics, the exponential of the Hamiltonian is a fundamental quantity. All methods for solving these problems compute, one way or another, (matrix elements of) the exponential of the matrix H. In the case of real-time quantum dynamics $x = -it/\hbar$ whereas for quantum statistical problems $x = -\beta = -1/k_B T$.

Formally, the exponential of a matrix H can be defined in terms of the Taylor series

$$e^{xH} = \sum_{n=0}^{\infty} \frac{x^n}{n!}H^n \quad , \tag{4}$$

just like if H would be a number. For most problems of interest, there won't be enough memory to store the matrix H (typical applications require matrices of dimension $10^5 \times 10^5$ or larger) and hence there also will be no memory to store the full matrix e^{xH}. So let us concentrate on the other extreme: The calculation of an arbitrary matrix element $\langle \psi | e^{xH} | \psi' \rangle$. Although from mathematical point of view, formal expansion (4) is all that is really needed, when it comes to computation, (4) is quite useless. The reason is not so much that it is a Taylor series but rather that it contains powers of the matrix, indicating that simply summing the terms in (4) may be very inefficient (and indeed it is).

There is one particular case in which it is easy to compute the matrix element $\langle \psi | e^{xH} | \psi' \rangle$ namely if *all* the eigenvalues and eigenvectors are known. Indeed, from (4) it follows that

$$e^{xH} | \Phi_j \rangle = \sum_{n=0}^{\infty} \frac{x^n}{n!} H^n | \Phi_j \rangle = \sum_{n=0}^{\infty} \frac{x^n}{n!} E_j^n | \Phi_j \rangle = e^{xE_j} | \Phi_j \rangle \quad , \tag{5}$$

where (here and in the following) E_n denotes the n-th eigenvalue of the matrix H and $| \Phi_n \rangle$ is the corresponding eigenvector. We will label the eigenvalues such that $E_0 \leq E_1 \leq \ldots \leq E_{M-1}$ where M is the dimension of the matrix H. From (5) is follows that

$$\langle \psi | e^{xH} | \psi' \rangle = \sum_{j=0}^{M-1} \langle \psi | \Phi_j \rangle \langle \Phi_j | \psi' \rangle e^{xE_j} \quad . \tag{6}$$

Of course, result (6) is almost trivial but it is important to keep in mind that, except for some pathological cases, there seems to be no other practical way to compute the matrix element $\langle \psi | e^{xH} | \psi' \rangle$ without making approximations (assuming H is a large matrix). In general we don't know the solution of the eigenvalue problem of the matrix H, otherwise we would already have solved the most difficult part of the whole problem. Therefore (6) is not of practical use.

Solving the time-dependent Schrödinger equation for even a single particle moving in a non-trivial (electromagnetic) potential is not a simple matter. The main reason is that for most problems of interest, the dimension of the matrix representing $\mathcal{H}$ is quite large and although the dimension of the matrices involved is certainly not as large as in the case of typical many-body quantum systems, exact diagonalization techniques are quite useless. Indeed, a calculation of the time-development of the wave function by exact diagonalization techniques requires the knowledge of *all* eigenvectors and *all* eigenvalues (i.e. $\approx 10^{13}$ Mb or more RAM to store these data). Thus, we need algorithms that do not use more than $\mathcal{O}(M)$ storage elements. Diagonalization methods that only require $\mathcal{O}(M)$ memory locations are of no use either because they can only compute a (small) part of the spectrum. Methods based on importance sampling concepts cannot be employed at all because there is

no criterion to decide which state is important or which is not: The "weight" of a state $e^{-itE_j/\hbar}$ is a complex number of "size" one.

Although from numerical point of view the TDSE looks like any other differential equation which one should be able to solve by standard methods (Runge-Kutta, ...) this is not the case. Standard methods are based on (clever) truncations of the Taylor series expansion. It is easy to convince oneself that, for the TDSE, this implies that these numerical algorithms do not conserve the norm of the wave function.[6] This, from physical point of view, is unacceptable because it means that during the numerical solution of the TDSE, the number of particles will change. Moreover, it can be shown[6] that this implies that these methods are not always stable with respect to rounding and other numerical errors. For completeness it should be mentioned that the Cranck-Nicholson algorithm does conserve the norm of the wave function and is unconditionally stable. However, except for one-dimensional problems, in terms of accuracy and efficiency it cannot compete with the algorithms to be discussed below.[6]

A key concept in the construction of an algorithm for solving the TDSE is the so-called unconditional stability. An algorithm for solving the TDSE is unconditionally stable if the norm of the wavefunction is conserved *exactly*, at *all* times.[6] From physical point of view, unconditional stability obviously is an essential requirement. If an algorithm is unconditionally stable the errors due to rounding, discretization etc. never run out of hand, irrespective of the choice of the grid, the time step, or the number of propagation steps. Recall that the formal solution of the TDSE is given by

$$|\Phi(m\tau)\rangle = e^{-im\tau H}|\Phi(t=0)\rangle \quad , \tag{7}$$

where $m = 0, 1, \ldots$ counts the number of time-steps τ. Here and in the following we absorb $\hbar$ in τ.

A simple, general recipe for constructing an unconditionally stable algorithm is to use unitary approximations to the (unitary) time-step operator $U(\tau) = e^{-i\tau H}$.[6] The Trotter-Suzuki product formula approach, to be discussed in the next section, provides the necessary mathematical framework for constructing unconditionally stable, accurate and efficient algorithms to solve the TDSE.[6]

3. Trotter-Suzuki formulae

In all cases that we know of, the Hamiltonian is a sum of several contributions and each contribution itself is usually simple enough so that we can diagonalize it ourselves by some (simple) transformation. The Hamiltonian for a particle in a potential provides the most obvious example: We can write the Hamiltonian as a sum of the free-particle Hamiltonian and a potential energy. It is trivial to diagonalize both parts independently but it is usually impossible to diagonalize the

sum.

The question we can now put ourselves is the following. Suppose we can diagonalize each of the terms in H by hand. Then, it is very reasonable to assume that we can also compute the exponential of each of the contributions separately (see the discussion in the previous section). Is there then a relation between the exponentials of each of the contributions to H and the exponential of H and if so, can we use it to compute the latter ?

The answer to this question is affirmative and can be found in the mathematical literature of the previous century. The following fundamental result due to Lie,[7] is the basis for the Trotter-Suzuki method for solving quantum problems.[8,9,10] It expresses the exponential of a sum of two matrices as infinite ordered product of the exponentials of the two individual matrices:

$$e^{x(A+B)} = \lim_{m\to\infty} \left(e^{xA/m} e^{xB/m} \right)^m \quad, \tag{8}$$

where, for our purposes, A and B are $M \times M$ matrices. The result (8) is called the Trotter formula.[11] Note that $e^{A+B} = e^A e^B$ **if and only if** the matrices A and B commute, i.e. $[A, B] = AB - BA = 0$.

A first hint for understanding why (8) holds comes from comparing the two Taylor series

$$
\begin{aligned}
e^{x(A+B)/m} &= I + \frac{x}{m}(A+B) + \frac{1}{2}\frac{x^2}{m^2}(A+B)^2 + \mathcal{O}(x^3/m^3) \\
&= I + \frac{x}{m}(A+B) \\
&\quad + \frac{1}{2}\frac{x^2}{m^2}(A^2 + AB + BA + B^2) + \mathcal{O}(x^3/m^3) \quad,
\end{aligned}
\tag{9a}
$$

and

$$e^{xA/m} e^{xB/m} = I + \frac{x}{m}(A+B) + \frac{1}{2}\frac{x^2}{m^2}(A^2 + 2AB + B^2) + \mathcal{O}(x^3/m^3) \quad. \tag{9b}$$

It is clear that for sufficiently large m, both expansions will agree up to terms of $\mathcal{O}(x^2\|[A,B]\|/m^2)$.[12] Thus, for sufficiently large m (how large depends on x and $\|[A,B]\|$),

$$e^{x(A+B)/m} \approx e^{xA/m} e^{xB/m} \quad. \tag{10}$$

A mathematically rigorous treatment shows that[13]

$$\|e^{x(A+B)/m} - e^{xA/m} e^{xB/m}\| \le \frac{x^2}{2m^2}\|[A,B]\| e^{|x|(\|A\|+\|B\|)/m} \quad, \tag{11}$$

demonstrating that for finite m, the difference between the exponential of a sum

of two matrices and the ordered product of the individual exponentials vanishes as x^2/m. As expected, (11) also reveals that this difference is zero if A and B commute: If $[A, B] = 0$ then $e^{x(A+B)} = e^{xA}e^{xB}$, as already mentioned above. For the case at hand $x = -im\tau$ and then the upperbound in (11) can be improved considerably to read[6]

$$\|e^{-i\tau(A+B)} - e^{-i\tau A}e^{-i\tau B}\| \leq \frac{\tau^2}{2}\|[A, B]\| \quad , \tag{12}$$

Except for the fact that we assumed that $H = A + B$, the above discussion has been extremely general. This suggests that one can apply the Trotter-Suzuki approach to a wide variety of problems and indeed one can. We have only discussed the most simple form of the Trotter formula. There now exist a vast number of extensions and generalizations of which we will consider only three of them.

The Trotter formula is readily generalized to the case of more than two contributions to H. Writing $H = \sum_{i=1}^{p} A_i$ it can be shown that[6,13]

$$\|e^{-i\tau(A_1+...+A_p)} - e^{-i\tau A_1}\dots e^{-i\tau A_p}\| \leq \frac{\tau^2}{2} \sum_{1\leq i<j\leq p} \|[A_i, A_j]\| \quad , \tag{13}$$

showing that *any* decomposition of the Hamiltonian qualifies as a candidate for applying the Trotter-Suzuki approach. This is an important conclusion because the flexibility of choosing the decomposition of H can be exploited to construct efficient algorithms. From the above discussion it is also clear that at no point, an assumption was made about the "importance" of a particular contribution to H. This is the reason why the Trotter-Suzuki approach can be used where perturbation methods break down.

The product formula (10) is the simplest one can think of. We use it to define an approximate time-step operator

$$U_1(\tau) = e^{-i\tau A_1}\dots e^{-i\tau A_p} \quad . \tag{14}$$

The hermitian conjugate of this operator is given by

$$U_1^\dagger(\tau) = e^{i\tau A_p}\dots e^{i\tau A_1} \quad , \tag{15}$$

from which it follows that

$$U_1(\tau)U_1^\dagger(\tau) = I \quad . \tag{16}$$

For simplicity we have assumed that H has be written as a sum of hermitian contributions, i.e. $A_i = A_i^\dagger$ for $i = 1, \dots, p$. Result (16) implies that $(U_1(\tau))^{-1} = U_1^\dagger(\tau)$ hence $U_1(\tau)$ is a unitary approximation to the time-step operator $e^{-i\tau H}$. Thus, if we succeed in implementing $U_1(\tau)$, the resulting algorithm will be unconditionally

stable by construction. The upperbound in (13) shows that the error made by replacing $e^{-i\tau H}$ by $U_1(\tau)$ will, in the worst case, never exceed a constant multiplied by τ^2. Therefore $U_1(\tau)$ is said to be a first-order approximant to the time-step operator.

For many applications it is necessary to employ an algorithm that is correct up to fourth order in the time step. Approximants correct up to second order are obtained by symmetrization[6,13,14]

$$U_2\left(\tau\right) = U_1^T(\tau/2)U_1\left(\tau/2\right) \quad , \tag{17}$$

where the U_1^T is the transpose of U_1 . Trotter-Suzuki formula-based procedures to construct algorithms that are correct up to fourth-order in the time step are given in ref.6. From practical point of view, a disadvantage of the fourth-order methods introduced in ref.6 is that they involve commutators of various contributions to the Hamiltonian. Recently Suzuki proposed a symmetrized fractal decomposition of the time evolution operator.[15] Using this formula, a fourth-order algorithm is easily built from a second-order algorithm by applying[15]

$$U_4(\tau) = U_2(p\tau)U_2(p\tau)U_2((1 - 4p)\tau)U_2(p\tau)U_2(p\tau) \quad , \tag{18}$$

where $p = 1/(4 - 4^{1/3})$ and $U_n(\tau)$ is the n–th order approximation to $U(\tau)$, i.e. $U(\tau) = U_n(\tau) + \mathcal{O}(\tau^{n+1})$. It is trivial to show that all of the above approximations are unitary operators, hence the corresponding algorithms will be unconditionally stable. Note that once we have programmed a first-order algorithm, writing the code to implement the second- and fourth-order algorithms will normally only take a few seconds. Finally we would like to emphasize that there are many different ways to construct and use higher-order Suzuki-formulae and that it is by no means clear that the ones used above lead to the most efficient algorithms for other kinds of TDSE problems. A systematic comparison of various schemes is given in Ref. 16

4. Implementation: Preliminaries

The translation of the rather formal description of the product-formula algorithms into a useful program is fairly straightforward and systematic. We will illustrate the main ingredients of this translation process by means of a simple example: A model describing the motion of a particle moving on a line of length X. In appropriate units the Hamiltonian is given by

$$\mathcal{H} = -\frac{d^2}{dx^2} + V(x) \quad , \tag{19}$$

where $V(x)$ represents the potential at position x. We will adopt free-end boundary

conditions in the following. This implies that a wave hitting the end points $x = 0$ or $x = X$ will be reflected with probability one. Thus, the wave function of the particle $\psi(x, t) = 0$ unless $0 < x < X$.

Obviously, numerical solution of (19) requires some discretization of continuum space. Let δ be the mesh length in the x-direction and approximate $\psi(x, t)$ by $\psi_l(t)$ for $(l - 1/2)\delta \leq x < (l + 1/2)\delta$. Since free-boundary conditions have been adopted, $\psi_l(t) = 0$ if $l < 1$ or $l > L + 1$. Replacing the second derivative with respect to x by its simplest finite-difference approximation $(d^2\psi(x, t)/dx^2 \approx \delta^{-2}[\psi_{l+1}(t) - 2\psi_l(t) + \psi_{l-1}(t)])$ yields the TDSE

$$\frac{\partial}{\partial t}\psi_l(t) = -i\{-\delta^{-2}\left[\psi_{l+1}(t) + \psi_{l-1}(t)\right] + v_l\psi_l(t)\} \quad , \tag{20}$$

with $v_l = V(l\delta) + 2\delta^{-2}$. In practice situations the number of mesh points $L + 1$ will be finite. Hence (20) can be written in matrix form

$$\frac{\partial\psi(t)}{\partial t} = -iH\psi(t) \quad , \tag{21}$$

where $\psi(t) = (\psi_1(t), ..., \psi_{L+1}(t))^T$ is a column vector of length $L + 1$ and H is the tri-diagonal matrix

$$H = \begin{pmatrix} v_1 & -\delta^{-2} & & & \\ -\delta^{-2} & v_2 & & & \\ & & \ddots & & \\ & & & v_L & -\delta^{-2} \\ & & & -\delta^{-2} & v_{L+1} \end{pmatrix} . \tag{22}$$

The numerical solution of the difference equation (20) will be an approximation to the solution of the TDSE with Hamiltonian (19). The accuracy of the approximation is, in this case, determined by the mesh length δ. By construction the approximate solution will converge to the continuum result if $\delta \to 0$, i.e. the numerical method is "consistent".[17]

Difference equation (20) can also be interpreted as the TDSE for a particle moving on a chain of $L + 1$ lattice sites. This analogy proves to be very valuable if the matrix representing the Hamiltonian takes a more complicated form than (22) (see Section 5). The Hamiltonian for the lattice model reads

$$\mathcal{H} = -t \sum_l \left(c_l^+ c_{l+1} + c_{l+1}^+ c_l\right) - W \sum_l \epsilon_l n_l \quad , \tag{23}$$

where c_l^+ (c_l) creates (annihilates) a particle at the site l, $n_l = c_l^+ c_l$ counts the number of particles at site l (i.e. $n_l = 0, 1$ since here there is at most one particle), V sets the kinetic energy scale and $W\epsilon_l$ is the potential at site l felt by the particle.

Although not essential (we are considering one particle only), the operators c_l^+ and c_l are taken to obey fermion operator algebra, i.e. $\{c_l^+, c_{l'}^+\} = \{c_l, c_{l'}\} = 0$ and $\{c_l^+, c_{l'}\} = \delta_{l,l'}$. A state $|\Phi(t)\rangle$ of this single-particle system can be written as

$$|\Phi(t)\rangle = \sum_{l=1}^{L+1} \Phi_l(t) c_l^+ |0\rangle \quad, \tag{24}$$

where $|0\rangle$ denotes the vacuum state. Substituting representation (24) in the TDSE

$$\frac{\partial \Phi(t)}{\partial t} = -iH\Phi(t) \quad, \tag{25}$$

with H given by (24) yields

$$\frac{\partial}{\partial t}\Phi_l(t) = -i\left\{ V\left[\Phi_{l+1}(t) + \Phi_{l-1}(t)\right] + W\epsilon_l\ \Phi_l(t)\right\} \quad; \quad l = 1,...,L+1 \quad, \tag{26}$$

and because of the free boundary conditions $\Phi_l(t) = 0$ if $l \leq 0$ or $l > L+1$. Comparison of (21) and (26) learns that both formulations are equivalent provided we set $V = -\delta^{-2}$ and $W\epsilon_l = v_l$.

The intimate relationship between discretized Schrödinger equation (21), matrix equation (22) and lattice model (25) shows that the latter, properly generalized to the d-dimensional case, may be regarded as a generic model, encompassing both genuine lattice models themselves as well as the (simplest) difference approximation to continuum problems.

In general there will be many possibilities to write down different decompositions of a given Hamiltonian. From theoretical point of view, the choice of the decomposition is arbitrary. In practice however, this flexibility can be exploited to considerable extent to tailor the algorithm to the computer architecture on which the algorithm will execute. Of particular interest are decompositions that vectorize well and have a large intrinsic degree of parallelism.

There are indeed many different possibilities to write the matrix

$$H = \begin{pmatrix} W\epsilon_1 & V & & & & \\ V & W\epsilon_2 & V & & & \\ & V & W\epsilon_3 & V & & \\ & & & \ddots & & \\ & & & V & W\epsilon_L & V \\ & & & & V & W\epsilon_{L+1} \end{pmatrix} \quad . \tag{27}$$

as a sum of "more simple" matrices. For practical purposes, only decompositions that lead to matrices that can be diagonalized by hand qualify because only then it is straightfoward to compute the exponential of these matrices. A convenient choice is to write the matrix as a sum of a diagonal matrix, and two block-diagonal

matrices made up of 2×2 matrices. More explicitly

$$H = H_0 + H_1 + H_2 \quad , \tag{28}$$

where

$$H_0 = \begin{pmatrix} W\epsilon_1 & 0 & & & & \\ 0 & W\epsilon_2 & 0 & & & \\ & 0 & W\epsilon_3 & 0 & & \\ & & & \ddots & & \\ & & & & W\epsilon_{L+1} \end{pmatrix} \quad , \tag{29}$$

$$H_1 = \begin{pmatrix} 0 & V & & & & \\ V & 0 & 0 & & & \\ & 0 & 0 & V & & \\ & & V & 0 & & \\ & & & & \ddots & \\ & & & & & 0 & 0 \end{pmatrix} \quad , \tag{30}$$

and

$$H_2 = \begin{pmatrix} 0 & 0 & & & & \\ 0 & 0 & V & & & \\ & V & 0 & & & \\ & & & \ddots & & \\ & & & & 0 & V \\ & & & & V & 0 \end{pmatrix} \quad . \tag{31}$$

It is easy to see that the exponential of a block matrix is itself a block matrix build from exponentials of 2×2 matrices that one can calculate by hand. For the present case, these plane rotation matrices take the form

$$M = \begin{pmatrix} \cos\tau|V| & -i\sin\tau|V| \\ -i\sin\tau|V| & \cos\tau|V| \end{pmatrix} \quad . \tag{32}$$

The first-order approximant to the time-step operator corresponding to decomposition (28) reads

$$U_1(\tau) = e^{-i\tau H_0} e^{-i\tau H_1} e^{-i\tau H_2} \quad . \tag{33}$$

From the general theory given above, it immediately follows how to build higher-order approximants with little extra effort.

Multiplication of an abitrary vector by the matrices $e^{-i\tau H_1}$ or $e^{-i\tau H_2}$ amounts to selecting the appropiate pair of elements of the vector and performing a plane rotation. Calculating the result of multiplying a vector and the diagonal matrix

$e^{-i\tau H_0}$ is almost trivial. Summarizing: we have shown that by chosing a suitable decomposition, the numerical solution of the TDSE for a single particle moving on a line has been reduced to repeated multiplications of the wave function by scalars and 2×2 matrices. The next section shows that with modest efforts (but unfortunately not without a more tedious notation) the same approach can be used to construct algorithms for a "complicated" TDSE.

5. Implementation: Details

This section illustrates how to use the concepts introduced above to the case of the TDSE for a charged (spinless) non-relativistic particle in an external, static magnetic field $\mathbf{B}$. The Hamiltonian reads

$$\mathcal{H} = \frac{1}{2m^*} \left(\mathbf{p} - e\mathbf{A} \right)^2 + V \quad , \tag{34}$$

where m^* is the effective mass of the particle with charge e, $\mathbf{p} = -i\hbar\nabla$ is the momentum operator, $\mathbf{A}$ represents the vector potential and V denotes the potential. For many applications it is sufficient to consider the choice $\mathbf{B} = (0, 0, B(x, y))$ and $V = V(x, y)$. Then the problem is essentially two-dimensional and the motion of the particle may be confined to the x–y plane. For numerical work, there is no compelling reason to adopt the Coulomb gauge ($\mathrm{div}\mathbf{A} = 0$). A convenient choice for the vector potential is $\mathbf{A} = (A_x(x, y), 0, 0)$ where

$$A_x(x, y) = -\int_0^y B(x, y)\, dy \quad . \tag{35}$$

We will solve the TDSE for the Hamiltonian (34) with the boundary condition that the wave function is zero outside the simulation box, i.e. we assume perfectly reflecting boundaries.

For computational purposes it is expedient to express all quantities in dimensionless units. Denoting the unit of length by λ (e.g. the Fermi wavelength, the de Broglie wavelength, ...), wavevectors are measured in units of $k = 2\pi/\lambda$, energies in $E = \hbar^2 k^2/2m^*$, time in $\hbar/E$ and the vector potential in $e\lambda/\hbar$. Expressed in these dimensionless variables Hamiltonian (34) reads

$$\mathcal{H} = -\frac{1}{4\pi^2} \left\{ \left[\frac{\partial}{\partial x} - iA_x(x, y) \right]^2 + \frac{\partial^2}{\partial y^2} \right\} + V(x, y) \quad . \tag{36}$$

An essential step in the construction of a numerical algorithm is to discretize the derivatives with respect to the x and y coordinates (of course, if the problem is defined on a lattice instead of in continuum space this step can be omitted). For many purposes, it is necessary to use a difference formula for the first and second derivatives in (36) that is accurate up to fourth order in the spatial mesh size δ.

Using the standard four and five point difference formula[18] the discretized r.h.s. of (36) reads

$$
\begin{aligned}
H\Phi_{l,k}(t) = \frac{1}{48\pi^2\delta^2} \Big\{ &\Big[1 - i\delta\big(A_{l,k} + A_{l+2,k}\big)\Big]\Phi_{l+2,k}(t) \\
&+ \Big[1 + i\delta\big(A_{l-2,k} + A_{l,k}\big)\Big]\Phi_{l-2,k}(t) \\
&- 16\Big[1 - \frac{i\delta}{2}\big(A_{l,k} + A_{l+1,k}\big)\Big]\Phi_{l+1,k}(t) \\
&- 16\Big[1 + \frac{i\delta}{2}\big(A_{l-1,k} + A_{l,k}\big)\Big]\Phi_{l-1,k}(t) \\
&+ \Phi_{l,k+2} + \Phi_{l,k-2} - 16\Phi_{l,k+1} - 16\Phi_{l,k-1}(t) \\
&+ \Big[60 + 12\delta^2 A_{l,k}^2 + 48\pi^2\delta^2 V_{l,k}\Big]\Phi_{l,k}(t) \Big\} + \mathcal{O}(\delta^5) \quad , \quad (37)
\end{aligned}
$$

where $\Phi_{l,k}(t) = \Phi(l\delta, k\delta, t)$ and $A_{l,k} = A_x(l\delta, k\delta)$. The discretized form (37) will provide a good approximation to the continuum problem if δ is substantially smaller than the smallest physical length scale. For the case at hand there are two such scales. One is the de Broglie wavelength of the particle (which by definition is equal to λ) and the other is the (smallest) magnetic length defined by $l_B^2 = \min_{(x,y)} |\hbar/eB(x,y)|$. From numerical calculations (not shown) it follows that $\delta = 0.1\min(1, l_B)$ yields a good compromise between accuracy and the CPU time required to solve the TDSE.

Straightforward application of the product-formula recipe to expression (37) requires a cumbersome matrix notation. This can be avoided by using the second-quantization language introduced in the previous section

Defining

$$
|\Phi(t)\rangle = \sum_{l=1}^{L_x}\sum_{k=1}^{L_y} \Phi_{l,k}(t) c_{l,k}^+ |0\rangle \quad , \tag{38}
$$

where L_x and L_y are the number of grid points in the x and y direction respectively and $c_{l,k}^+$ creates a particle at lattice site (l, k), (38) can be written as

$$
|\Phi(m\tau)\rangle = e^{-im\tau H}|\Phi(t = 0)\rangle \quad , \tag{39}
$$

where

$$
\begin{aligned}
H = \frac{1}{48\pi^2\delta^2} \sum_{l=1}^{L_x-2}\sum_{k=1}^{L_y} \Big\{ &\Big[1 - i\delta\big(A_{l,k} + A_{l+2,k}\big)\Big]c_{l,k}^+ c_{l+2,k} \\
&+ \Big[1 + i\delta\big(A_{l,k} + A_{l+2,k}\big)\Big]c_{l+2,k}^+ c_{l,k} \Big\}
\end{aligned}
$$

$$-\frac{1}{3\pi^2\delta^2}\sum_{l=1}^{L_x-1}\sum_{k=1}^{L_y}\left\{\left[1-\frac{i\delta}{2}\left(A_{l,k}+A_{l+1,k}\right)\right]c_{l,k}^+c_{l+1,k}\right.$$

$$\left.+\left[1+\frac{i\delta}{2}\left(A_{l,k}+A_{l+1,k}\right)\right]c_{l+1,k}^+c_{l,k}\right\}$$

$$+\frac{1}{48\pi^2\delta^2}\sum_{l=1}^{L_x}\sum_{k=1}^{L_y-2}\left(c_{l,k}^+c_{l,k+2}+c_{l,k+2}^+c_{l,k}\right)$$

$$-\frac{1}{3\pi^2\delta^2}\sum_{l=1}^{L_x}\sum_{k=1}^{L_y-1}\left(c_{l,k}^+c_{l,k+1}+c_{l,k+1}^+c_{l,k}\right)$$

$$+\frac{1}{48\pi^2\delta^2}\sum_{l=1}^{L_x}\sum_{k=1}^{L_y}\left(60+12\delta^2A_{l,k}^2+48\pi^2\delta^2V_{l,k}\right)+\mathcal{O}(\delta^5)\quad,\qquad(40)$$

where $c_{l,k}$ annihilates a particle at lattice site (l,k).

Hamiltonian (40) describes a particle that moves on a two-dimensional lattice by making nearest and next-nearest neighbor jumps. This interpretation suggests that H should be written as a sum of terms that represent groups of independent jumps.[6] A convenient choice is

$$A_1=\frac{1}{48\pi^2\delta^2}\sum_{l\in X_1}\sum_{k=1}^{L_y}\left\{\left[1-i\delta\left(A_{l,k}+A_{l+2,k}\right)\right]c_{l,k}^+c_{l+2,k}\right.$$

$$\left.+\left[1+i\delta\left(A_{l,k}+A_{l+2,k}\right)\right]c_{l+2,k}^+c_{l,k}\right\}\quad;$$

$$X_1=\{1,2,5,6,9,10,\ldots\}\quad,$$

$$A_2=\frac{1}{48\pi^2\delta^2}\sum_{k=1}^{L_y}\sum_{l\in X_2}\left\{\left[1-i\delta\left(A_{l,k}+A_{l+2,k}\right)\right]c_{l,k}^+c_{l+2,k}\right.$$

$$\left.+\left[1+i\delta\left(A_{l,k}+A_{l+2,k}\right)\right]c_{l+2,k}^+c_{l,k}\right\}\quad;$$

$$X_2=\{3,4,7,8,11,12,\ldots\}\quad,$$

$$A_3=\frac{-1}{3\pi^2\delta^2}\sum_{k=1}^{L_y}\sum_{l\in X_3}\left\{\left[1-\frac{i\delta}{2}\left(A_{l,k}+A_{l+1,k}\right)\right]c_{l,k}^+c_{l+1,k}\right.$$

$$\left.+\left[1+\frac{i\delta}{2}\left(A_{l,k}+A_{l+1,k}\right)\right]c_{l+1,k}^+c_{l,k}\right\}\quad;$$

$$X_3=\{1,3,5,7,9,11,\ldots\}\quad,$$

$$A_4=\frac{-1}{3\pi^2\delta^2}\sum_{k=1}^{L_y}\sum_{l\in X_4}\left\{\left[1-\frac{i\delta}{2}\left(A_{l,k}+A_{l+1,k}\right)\right]c_{l,k}^+c_{l+1,k}\right.$$

$$+\left[1+\frac{i\delta}{2}\left(A_{l,k}+A_{l+1,k}\right)\right]c_{l+1,k}^{+}c_{l,k}\right\} \quad ;$$
$$X_4 = \{2, 4, 6, 8, 10, 12, \ldots\} \quad ,$$

$$A_5 = \frac{1}{48\pi^2\delta^2}\sum_{k\in X_5}\sum_{l=1}^{L_x}\left(c_{l,k}^{+}c_{l,k+2}+c_{l,k+2}^{+}c_{l,k}\right) \quad ; \quad X_5 = \{1, 2, 5, 6, 9, 10, \ldots\} \quad ,$$

$$A_6 = \frac{1}{48\pi^2\delta^2}\sum_{k\in X_6}\sum_{l=1}^{L_x}\left(c_{l,k}^{+}c_{l,k+2}+c_{l,k+2}^{+}c_{l,k}\right) \quad ; \quad X_6 = \{3, 4, 7, 8, 11, 12, \ldots\} \quad ,$$

$$A_7 = \frac{-1}{3\pi^2\delta^2}\sum_{k\in X_3}\sum_{l=1}^{L_x}\left(c_{l,k}^{+}c_{l,k+1}+c_{l,k+1}^{+}c_{l,k}\right) \quad ; \quad X_3 = \{1, 3, 5, 7, 9, 11, \ldots\} \quad ,$$

$$A_8 = \frac{-1}{3\pi^2\delta^2}\sum_{k\in X_4}\sum_{l=1}^{L_x}\left(c_{l,k}^{+}c_{l,k+1}+c_{l,k+1}^{+}c_{l,k}\right) \quad ; \quad X_4 = \{2, 4, 6, 8, 10, 12, \ldots\} \quad ,$$

$$A_9 = \frac{1}{48\pi^2\delta^2}\sum_{k=1}^{L_y}\sum_{l=1}^{L_x}\left(60+12\delta^2 A_{l,k}^2+48\pi^2\delta^2 V_{l,k}\right)c_{l,k}^{+}c_{l,k} \quad , \tag{41}$$

and

$$U_1(\tau) = \prod_{n=1}^{9} e^{-i\tau A_n} \quad , \tag{42}$$

is the first-order approximant from which the algorithm, correct up to fourth-order in the spatial (δ) and temporal (τ) mesh size, can be build.

The rather formal language used above readily translates into a computer program. The first-order approximant (42) is implemented as follows. First we note that (42) actually means

$$U_1(\tau) = e^{-i\tau A_1}e^{-i\tau A_2}e^{-i\tau A_3}e^{-i\tau A_4}e^{-i\tau A_5}e^{-i\tau A_6}e^{-i\tau A_7}e^{-i\tau A_8}e^{-i\tau A_9} \quad . \tag{43}$$

To compute the result of letting $e^{-i\tau A_9}$ act on the wave function (i.e. a complex-valued vector of length M), we use the fact that all terms in the double sum, appearing in the expression of A_9 (see (43)), commute with each other and that A_9 is a diagonal matrix. Therefore one only has to multiply each element (k, l) of the vector by the corresponding element of A_9:

$$\Phi_{l,k} \leftarrow e^{-i\tau(60+12\delta^2 A_{l,k}^2+48\pi^2\delta^2 V_{l,k})/48\pi^2\delta^2}\Phi_{l,k} \quad . \tag{44}$$

Inspection of A_n for $n = 1, \ldots, 8$ shows that for fixed n, each of the terms in each double sum commutes with all the other terms in the same sum. This is because each of these terms corresponds to a jump of the particle between a pair

of two, isolated sites. For the purpose of implementation, this feature is of extreme importance.[6] To illustrate this point it is sufficient to consider the first of the exponents in (43) and use the fact that all terms commute to rewrite it as

$$
e^{-i\tau A_1} = \prod_{k=1}^{L_y} \prod_{l \in X_1} \exp\left(\frac{-i\tau}{48\pi^2\delta^2}\left\{\left[1 - i\delta\left(A_{l,k} + A_{l+2,k}\right)\right]c^+_{l,k}c_{l+2,k}\right.\right.
$$

$$
\left.\left. + \left[1 + i\delta\left(A_{l,k} + A_{l+2,k}\right)\right]c^+_{l+2,k}c_{l,k}\right\}\right) \quad . \quad (45)
$$

Furthermore, each of the exponents in the product (45) describes a two-site system, and the exponent of the corresponding two-by-two matrix can be worked out analytically.[6] In general

$$
\exp\left(i\tau\alpha c^+_{l,k}c_{l',k'} + i\tau\alpha^* c^+_{l',k'}c_{l,k}\right) = \left(c^+_{l,k}c_{l,k} + c^+_{l',k'}c_{l',k'}\right)\cos\tau|\alpha|
$$

$$
+ i\left(\alpha^{*-1}c^+_{l,k}c_{l',k'} + \alpha^{-1}c^+_{l',k'}c_{l,k}\right)\sin\tau|\alpha| \quad (46)
$$

Accordingly, the operation of $e^{-i\tau A_1}$ on a wave function can be computed as follows. For each pair of indices (k,l), get the two corresponding vector elements $\Phi_{l,k}$ and $\Phi_{l+2,k}$. and perform a plane rotation:

$$
\begin{pmatrix} \Phi_{l,k} \\ \Phi_{l+2,k} \end{pmatrix} \leftarrow \begin{pmatrix} \cos\tau|\alpha| & i\alpha^{-1}\sin\tau|\alpha| \\ i\alpha^{*-1}\sin\tau|\alpha| & \cos\tau|\alpha| \end{pmatrix} \begin{pmatrix} \Phi_{l,k} \\ \Phi_{l+2,k} \end{pmatrix} \quad , \quad (47)
$$

It is not difficult to see that $A_2, \ldots, A_8$ can be handled in exactly the same manner: One only has to pick other pairs of $\Phi_{l,k}$'s and repeat the steps outlined above.

Summarizing: Advancing the wave function by one time step has been reduced to a (large) number of 2×2 matrix-vector operations and one vector-vector operation. The computation of each of the nine factors can be done entirely parallel, fully vectorized, or mixed parallel and vectorized depending on the computer architecture on which the code will execute. Other technical details on the implementation of this algorithm can be found elsewhere.[19]

6. Data analysis

The amount of data generated by a TDSE solver can be tremendous: The wave function is known at each time step so that in principle the TDSE solver can generate $\mathcal{O}(16mM)$ bytes of data in a single run of m time steps. In typical applications, $M \approx 10^6$ and $m > 1000$. Clearly it may be difficult to store all these data. Therefore it is more appropriate to process the data as it is generated and compress it as much as possible.

A very appealing method to look at the data is to make say 100 snapshots of the (coarse grained) probability distribution and to use visualization techniques to

produce digital video's. Simply looking at these video's can already bring a lot of insight but, to be on the save side, this insight should be confronted with the results of more advanced, numerical processing of the data.

The numerical processing of the raw data generated by the TDSE solver depends to considerable extent on the details of the actual application. Therefore I will not dwell on this subject in full generality but confine myself to a discussion of a simple, widely applicable method to extract from the raw data, information about the spectrum of the model Hamiltonian.

Consider the matrix element $\langle \Phi(t=0)|\Phi(t)\rangle$ and write $|\Phi(t)\rangle$ in terms of the (unknown) eigenvalues and eigenvectors of H to obtain

$$f(t) \equiv \langle \Phi(t=0)|\Phi(t)\rangle = \sum_{j=0}^{M-1} |\langle \Phi(t=0)|\Phi_j\rangle|^2 e^{-itE_j} \quad . \tag{48}$$

From (48) it is clear that the Fourier transform of $f(t)$ with respect to t will give direct information on all the E_j's for which the overlap $|\langle \Phi(t=0)|\Phi_j\rangle|^2$ is not negligible. In other words, if we keep all the values of $f(t = m\tau)$ and compute the its Fourier transform, we obtain the local (with respect to the initial state $\Phi(t=0)$) density of states.

7. Applications

Trotter-Suzuki based TDSE solvers have been employed to study a variety of problems including wave localization in disordered and fractals,[6,20] electron emission from nanotips,[21,22,23] Andreev reflection in mesoscopic systems,[24,25] the Aharonov-Bohm effect,[26,27] quantum interference of charged identical particles,[28,27] etc.. Appealing features of the TDSE approach are that is extremely flexible in the sense that it can handle arbitrary geometries and (vector) potentials and that its numerical stability and accuracy are such that for all practical purposes the solution is exact.

Trotter-Suzuki formula-based algorithms can and also have been used to solve the TDSE for many-body quantum systems, including a 26-site S=1/2 Heisenberg model,[29] Ising models with a time-dependent transverse field,[30] spin-1/2 clusters in time-dependent magnetic fields,[31] and a spin-boson model.[32] The application of the TDSE approach is mainly limited by the storage needed for the (complex valued) wave function.

7.1 Electron Focussing[33]

Many important applications of optics heavily rely on the availability of sources that produce coherent and focussed beams of light. Likewise, for a wide variety of applications, it is of great interest to have sources that emit coherent and focussed beams of electrons. The simplest method for focussing electrons is to apply a large voltage between the source and the screen (or detector). Electrons leaving the source will be accelerated and provided this acceleration is sufficiently large, the width of the electron wave packet in the direction perpendicular to the direction of acceleration will be neglegible. This focussing mechanism is used in for instance television displays and conventional electron microscopes and can be entirely understood within a classical mechanical framework.

Another fairly common method to produce focussed beams (of water, air, ...) is to reduce the size of the aperture of the source. This technique works well as long as this size is much larger than the typical wavelength of the emitted particles. Once the dimension of the aperture becomes comparable to the characteristic wavelength of the particles, diffraction effects can have a dramatic influence on the direction of the emitted particles: The beam will no longer be collimated but will be spread out.

Recent experiments on atom-size tips[3,4] have demonstrated that they act as unusual electron beam sources, emitting electrons at fairly low applied voltages (a few thousand volts or less) with a small angular spread (of a few degrees). These properties make such electron sources very attractive for applications to electron holography and electron interferometry.[34−38] Extensive theoretical work[21,39] revealed that tunneling through the metal-vacuum potential is the main physical mechanism determining the unusual properties of the emitted electron beams.

Tunneling through a potential barrier is only one of the mechanisms for collimating an electron beam. It has been suggested[40] that adiabatic mode selection[41−43] is mainly responsible for the peculiar properties of the electron beams emitted from atom-size tips. The key ingredient of this description is the presence of a slowly varying, horn-like structure in the potential surrounding the tip and the assumption that the electron wave propagates adiabatically in this structure. However, the application of these ideas to the atom-size tips seems unjustified.[44,45]

Recent progress in manufacturing nanometre structures in two-dimensional electron gas (2DEG) systems have made it possible to perform "electron-optics" experiments in solid state devices.[46] In an ideal device the motion of the electrons is not affected by interactions with impurities, phonons etc., i.e. the electrons travel ballistically, just as they would do in ultra-high vacuum. In real devices, typical distances for ballistic motion can be as large as $250\lambda_F$, λ_F being the Fermi wavelength of the electrons.[47] From the viewpoint of field-electron emission, motion in the vacuum region is replaced by ballistic motion in the solid. Just as for the

electron-beam sources, it is of interest to explore the possibility of focussing (colli-mating) electrons in the solid.[1] It has been demonstrated that magnetic fields[47−49] or an electrostatic lens[50] can be used to focus the electrons. Furthermore it has been argued[47,51] that the rounding of the entrance/exit plane of a quantum point contact may act as a horn, leading to the collimation of the electron waves.

Electron waves emitted by atom-size tips are collimated to a much greater extent (a few degrees) than those produced by quantum point contacts. This is only partially due to the presence of the applied electric field which accelerates the electron when it emerges from the tip over a macroscopic distance. In the discussion that follows the "classical" collimation due to the acceleration will not be taken into account in order to allow a fair comparison of the various focussing mechanisms.

The atom-size tips and the quantum-point-contacts are both examples of elec-tron sources for which the emission area is comparable to the wavelength (de-noted by λ_F) of the emitted particles. In this section we present some results of a computer-simulation that have been instrumental to identify the physical mech-anisms by which electrons emitted by extremely small sources can be focussed. A more comprehensive account can be found elsewhere.[23]

The most direct approach to explore the properties of electrons emitted by these small structures is to simulate the motion of the electron waves by numerically solving the time-dependent Schrödinger equation. The main advantages of the TDSE approach are that is flexible in the sense that it can handle arbitrary geometries and potentials and therefore provides a unified framework to investigate and compare various focussing mechanisms, and that the results are, for all practical purposes, exact.

The focussing capability of a source is characterized as follows. Imagine a wave, with a well-defined direction, wavelength λ_F and energy E_F, leaving the source. A detector is placed far away from the latter. The (normalised) transmitted intensity $P(\theta)$ recorded by this detector is plotted as a function of the angle (θ) with respect to the normal to the exit plane of the source. The collimation is characterized by determining the largest angles for which $P(\theta_{1,2}) = 1/e$, $\theta_1 < 0$ and $\theta_2 > 0$. By definition, the angular spread $\theta_s \equiv |\theta_1 - \theta_2|/2$.

Typically we solve the TDSE on a grid of 1024×513 points with mesh size $\delta = \lambda_F/10$, using a time step $\tau = 0.03125\hbar/E_F$ where E_F is the Fermi energy, and 4096 time steps. Incident waves were chosen to be Gaussians of width $6\lambda_F \times 6\lambda_F$, sufficiently large to mimic a plane wave front impinging on the emission area. The angular distribution of intensity of the transmitted wave $P(\theta)$ is calculated by the method described in Ref.45. Simulations (not shown) demonstrate that the angular spread does not change if the width of the Gaussian is increased further.

The simplest model of a small source consists of a hard wall, reflecting the wave, with a small aperture in it. Such a constriction acts as a waveguide. Waves emerging from the small opening scatter strongly. This is illustrated in Fig.1 for
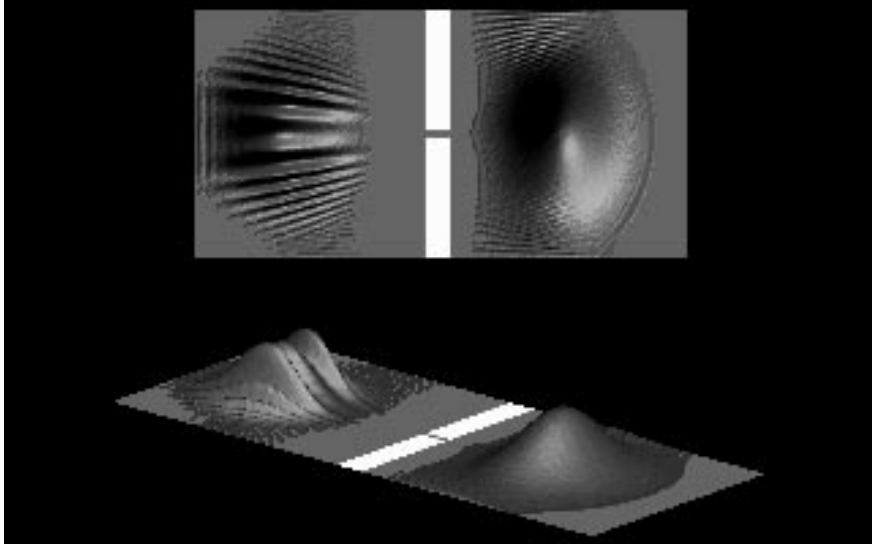
Fig.1. Intensity of the wave packet reflected and transmitted by a λ_F-wide aperture. The length of the constriction is $5\lambda_F$. The initial wave packet moves from the left to the right. The angular spread $\theta_s \approx 35°$. The emitted beam is not focused.

the case where the direction of the incident wave packet ψ is perpendicular to the hard wall, i.e. $\psi = 0°$. From Table 1, it follows that the angular spread θ_s strongly depends on the width W but little on the length L of the constriction, as one would expect on the basis of standard diffraction theory.[52]
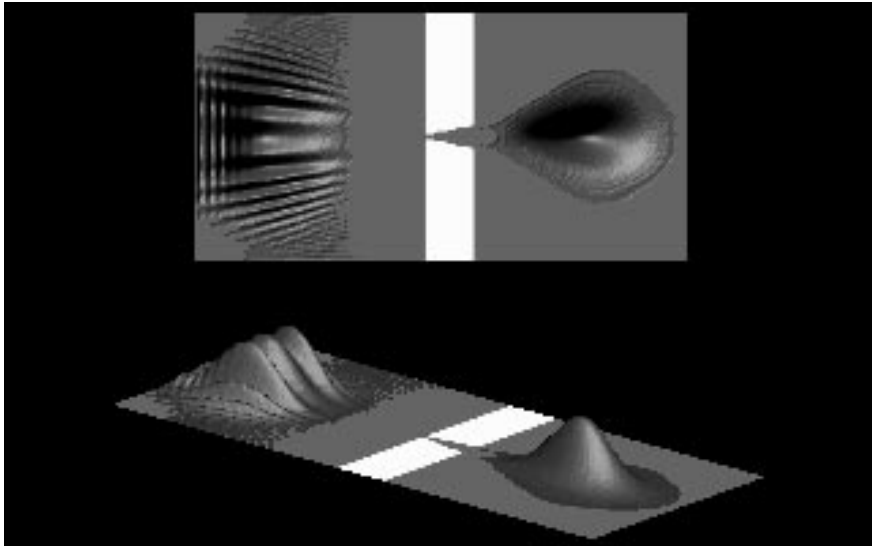
Fig.2. Intensity of the wave packet reflected and transmitted by a horn. The entrance plane is λ_F wide, the exit plane is $4.5\lambda_F$ wide, the constriction is $\lambda_F/2$ long and the total length of the device is $10\lambda_F$. The angular spread $\theta_s \approx 10°$.

Table 1. Influence on the angular spread θ_s of the width W and length L of the constriction. The angle of incidence $\psi = 0°$.

L/λ_F	W/λ_F	θ_s
1/2	1/2	42°
1/2	1	34°
1/2	2	18°
1	2	32°
5	2	32°

Gradually increasing the width of the opening in the hard wall yields a waveguide that looks like a horn. As illustrated in Fig.2 for the case of normal incidence ($\psi = 0°$), horns collimate waves but strong focussing requires relatively long horns.[45] This focussing mechanism is of secondary importance to the case of atom-size electron-emission tips.

It has been suggested[51] that a judiciously chosen potential inside a constriction can also provide a mechanism for focussing the wave. Table 2 demonstrates that this is not the case. A potential barrier inside the constriction does not focus the emitted wave but reduces its intensity. Comparing Fig.3 with Fig.1, it is clear that the presence of a potential inside the constriction does not lead to a change of the shape of the transmitted wave packet.
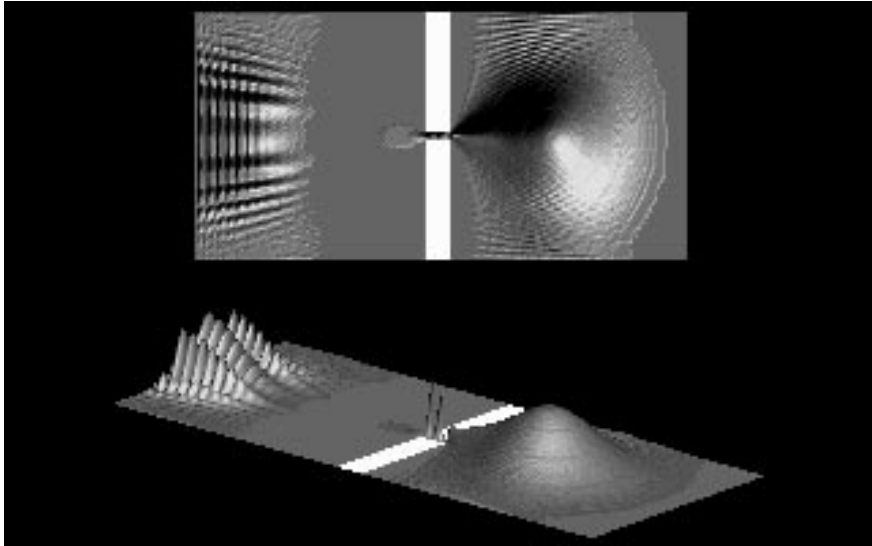
Fig.3. Intensity of the wave packet reflected and transmitted by a λ_F-wide aperture. The angle of incidence $\psi = 0°$. The length of the constriction is $5\lambda_F$, the height of the potential barrier inside the constriction is $0.95E_F$. The angular spread $\theta_s \approx 35°$. The emitted beam is not focussed.
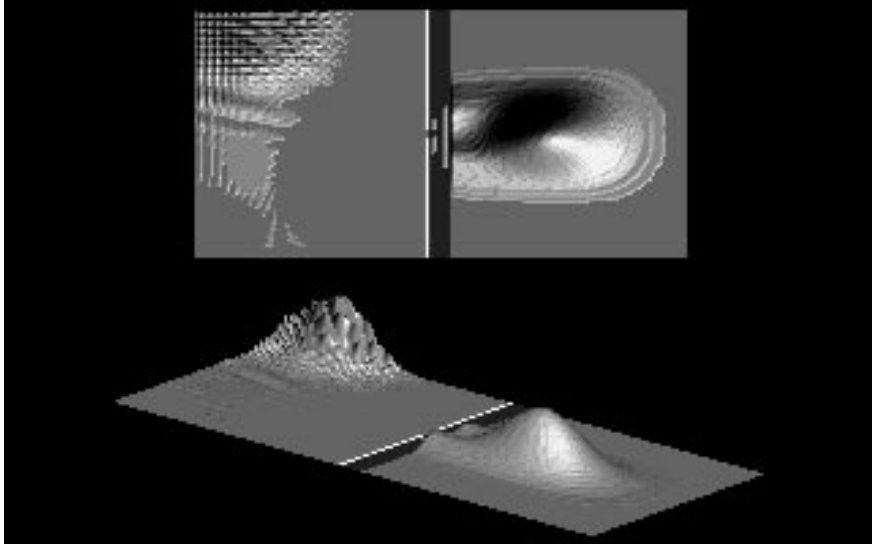
Fig.4. Intensity of the wave packet reflected and transmitted by a λ_F-wide aperture followed by a rectangular potential barrier. The length of the constriction is $\lambda_F/2$, the height and lenght of the potential barrier are $0.98E_F$ and $4.5\lambda_F$ respectively. The angle of incidence $\psi = 20°$. The angular spread $\theta_s \approx 10°$. The emitted beam is well-focussed.

Table 2. Influence on the angular spread θ_s of the presence of a constant potential V inside a single λ_F-wide constriction. The angle of incidence $\psi = 0°$.

V/E_F	θ_s
0.00	$34° \pm 4°$
0.75	$34° \pm 4°$
0.98	$33° \pm 4°$
1.00	$34° \pm 4°$

However, as shown in Fig.4 a rectangular barrier placed behind the constriction focusses the emitted wave at the cost of transmitted intensity. Long barriers of height slightly lower than the energy of the incident wave have optimal focussing properties and high efficiency.

The angular distribution of waves emitted by strongly focussing sources does not change much if the angle of incidence of the incident wave is varied. Comparing the simulation for the model used in Fig.4 for an angle of incidence of $\psi = 20°$ (not shown) instead of $\psi = 0°$, the outgoing waves only differ in the total transmitted intensity. The angular distributions are almost identical.

The simplest two-dimensional model of a single-atom tip consists of a constric-
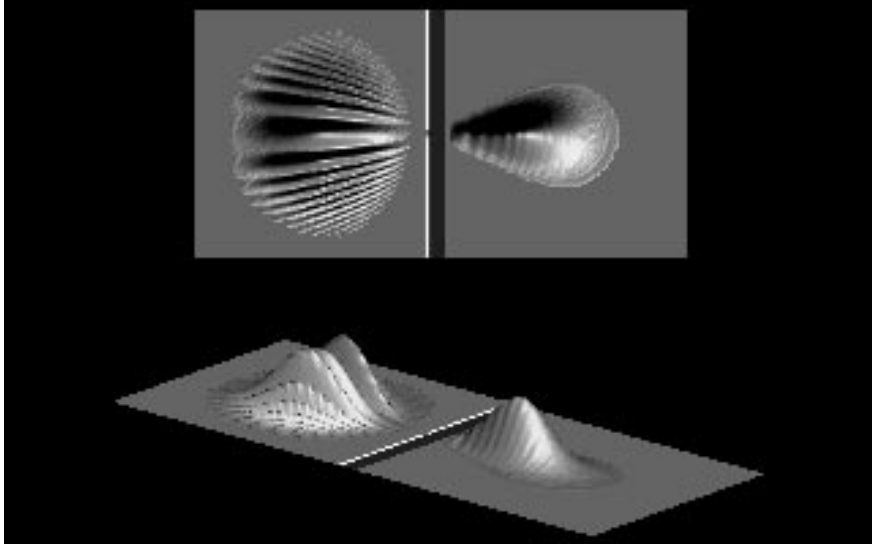
Fig.5. Intensity of the wave packet reflected and transmitted by a λ_F-wide aperture followed by a triangular potential barrier. The length of the constriction is $\lambda_F/2$, the height and lenght of the potential barrier are $1.5E_F$ and $5\lambda_F$ respectively. The angle of incidence $\psi = 0°$. The angular spread $\theta_s \approx 7°$. The emitted beam is strongly focussed.
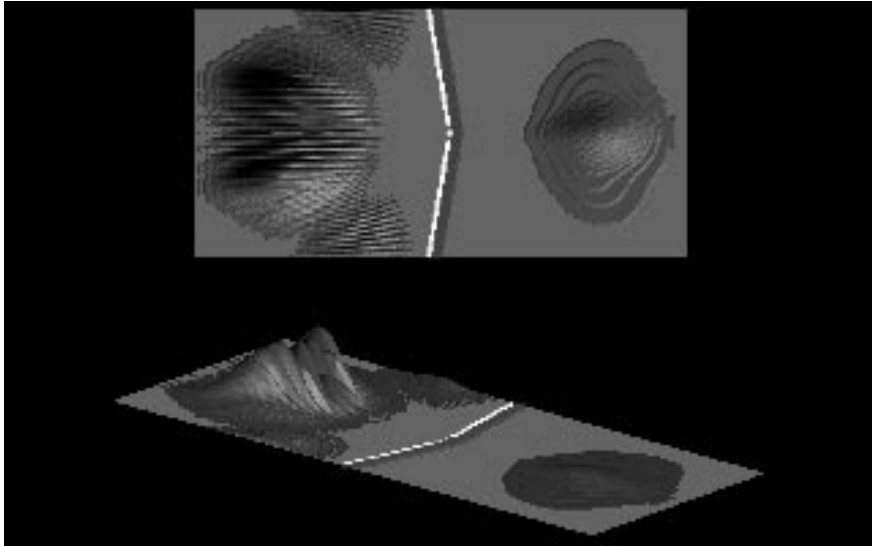
Fig.6. Intensity of the wave packet reflected and transmitted by a blunt tip. The angle of incidence $\psi = 0°$. The waves emerging from the two apertures merge to form one wave packet.

tion (the atom) followed by a triangular barrier (the metal-vacuum potential). Experimentally, the triangular barrier is higher than the energy of the waves inside the source. To leave the source the electron has to tunnel through the barrier. Fig.5

demonstrates that tunneling is a very effective focussing mechanism but strongly reduces the intensity of the emitted beam.
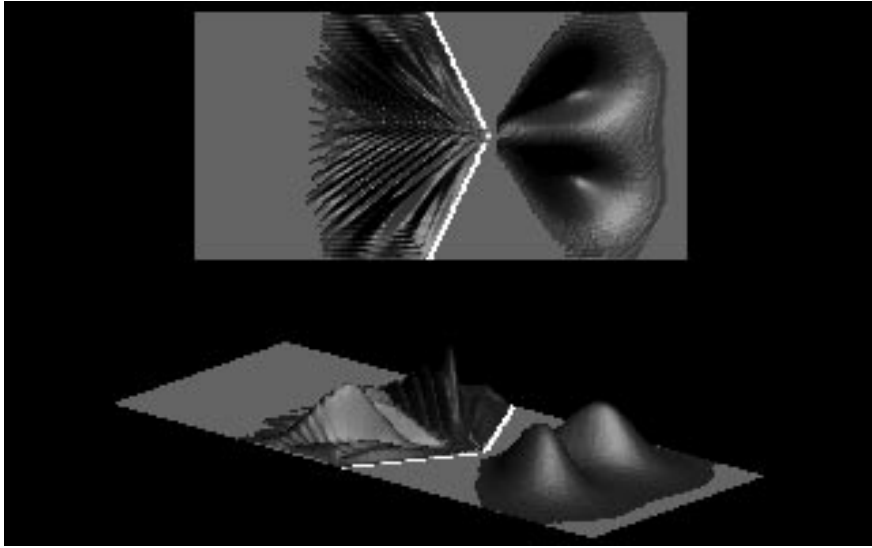
Fig.7. Intensity of the wave packet reflected and transmitted by a sharp tip. The angle of incidence $\psi = 0°$. The two coherent waves emitted by the two atoms do not merge. This source acts as a beam splitter.

Electron emission from three-atom tips crucially depend on the geometry of the tip. Simulations using two-dimensional models for these tips illustrate that the emission characteristics of a blunt and sharp tip are completely different. A two-dimensional blunt tip is modeled by a slightly deformed potential of two parallel constrictions (the two atoms) followed by a triangular barrier. The simulation result for the blunt tip, shown in Fig.6, illustrates that the two wave packets emerging from the two openings, merge to form one wave. According to the angular distribution on a screen placed far away from the source (not shown), this wave would give rise to a central spot and some background intensity, in qualitative agreement with experiment.[39] Further deformation of the potential modeling the blunt tip yields a potential representing a sharp (teton) tip. The wave packets emitted by this source differ considerably from those produced by the blunt tip. Indeed, Fig.7 shows that the sharp tip acts as a beam splitter, emitting two coherent electron waves, also in qualitative agreement with experiment.[39] In absence of a triangular barrier, the properties of the emitted wave do not resemble those of a sharp tip, as illustrated in Fig.8.

To summarize: A constriction followed by a suitable potential barrier constitutes the minimal model for describing the emission of focussed and coherent waves from very small sources.
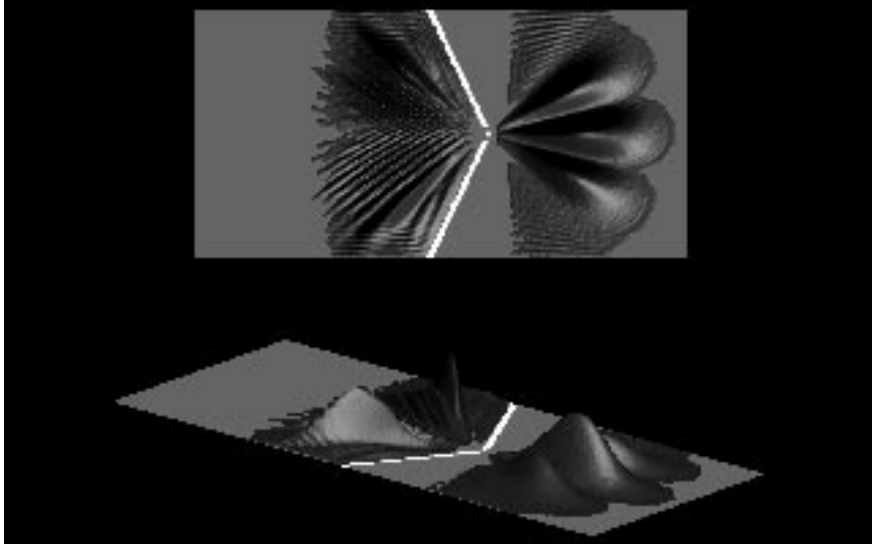
Fig.8. Intensity of the wave packet reflected and transmitted by a sharp tip, in the absence of the triangular barrier. The angle of incidence $\psi = 0°$. There is no evidence for of focussed electron emission.

7.2 Andreev Reflection[53]

Consider an experiment, sketched in Fig.9, on normal-metal – superconductor sandwich. Electrons move from the left (the normal metal) to the right (super-conductor). An electron with an energy (relative to the Fermi energy) smaller than the energy gap of the superconductor can only enter the superconductor if it can pick up another electron to form a pair. By doing so it leaves a hole behind. The hole moves backward (in time) with respect to the incident electrons and carries a charge $+e$. Therefore, in this simple picture, the conductivity through the metal-superconductor interface is enhanced by a factor of two. The electron-hole conversion at the normal-metal – superconductor interface is known as Andreev reflection[54,55].

The effect of diffraction on the electron-hole conversion can be studied by adding to the device depicted in Fig.9, a quantum point contact (QPC) with a width $W \approx \lambda_F$.[56] The electron approaches the QPC from the left. Part of the electron wave will pass through the constriction, the remaining part being reflected. The electron wave leaving the QPC is scattered in various directions but travels ballistically towards the superconductor. The hole wave travels towards the QPC. As a hole carries charge $+e$ and moves in the direction opposite to the incident electron wave, the part of hole wave that is transmitted by the QPC will enhance the conductance of the device.

When the relevant length scales of the device are of the order of a few λ_F, the physical picture used to interpret experiments[57] on systems that operate in the
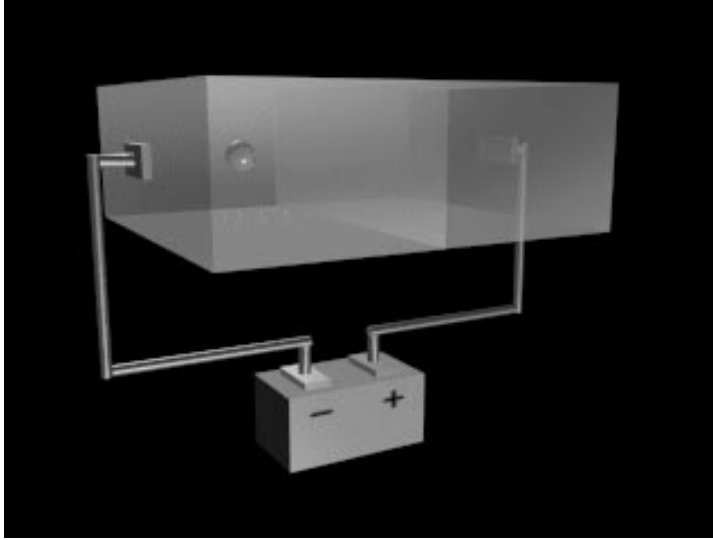
Fig.9. Schematic view of the experimental setup to study Andreev reflection in a nano-scale normal-metal – superconductor device.
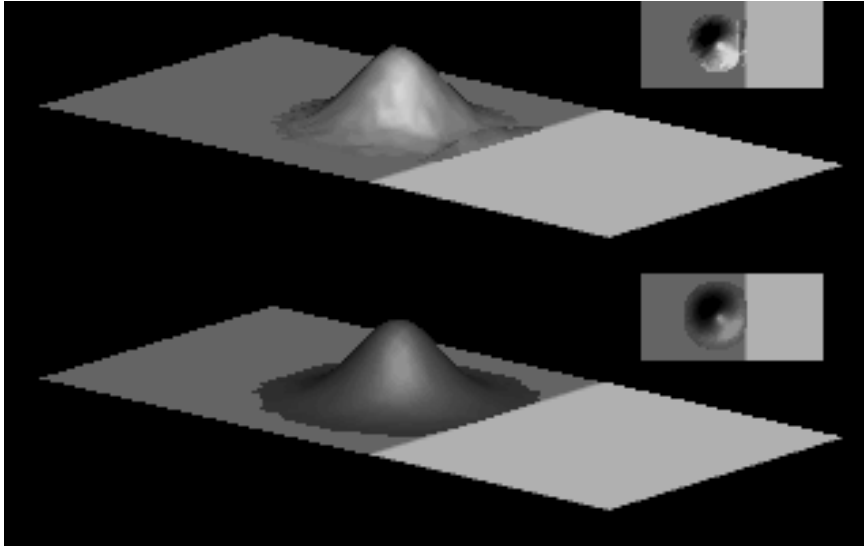
Fig.10. Two views of a snapshot of the electron (upper part) and hole (lower part) intensity taken at $t = 160\hbar/E_F$ for an unconventional superconductor with gap $\Delta = E_F$. Both the electron and hole wave are moving to the left. Initially, at $t = 0$, the electron wave moves to the right. Normal metal: Dark gray area; Superconductor: Light gray area.

classical ballistic limit does no longer apply. The most important new features, absent in the classical case, are wave mechanical effects such as diffraction by the QPC, scattering by impurities or corrugation of the N – S interface.

The effect of all these quantum phenomena on the charge transport through the

QPC can be investigated by solving the appropriate extension of the TDSE, namely the Bogoliubov-de Gennes equations[58]

$$i\hbar\frac{\partial}{\partial t}\begin{pmatrix} \psi(r,t) \\ \phi(r,t) \end{pmatrix} = \begin{pmatrix} \frac{(p-eA)^2}{2m^*} + V(r) & \Delta(r) \\ \Delta(r) & -\frac{(p+eA)^2}{2m^*} - V(r) \end{pmatrix}\begin{pmatrix} \psi(r,t) \\ \phi(r,t) \end{pmatrix} \quad , \quad (49)$$

where $\psi(r,t)$ and $\phi(r,t)$ denote the electron and hole wave function respectively, m^* is the effective mass, p is the momentum operator, e is the charge, $A = A(r)$ is the vector potential corresponding to an external magnetic field, $V(r)$ is the potential defining the geometry of the device and $\Delta(r)$ is the gap function.
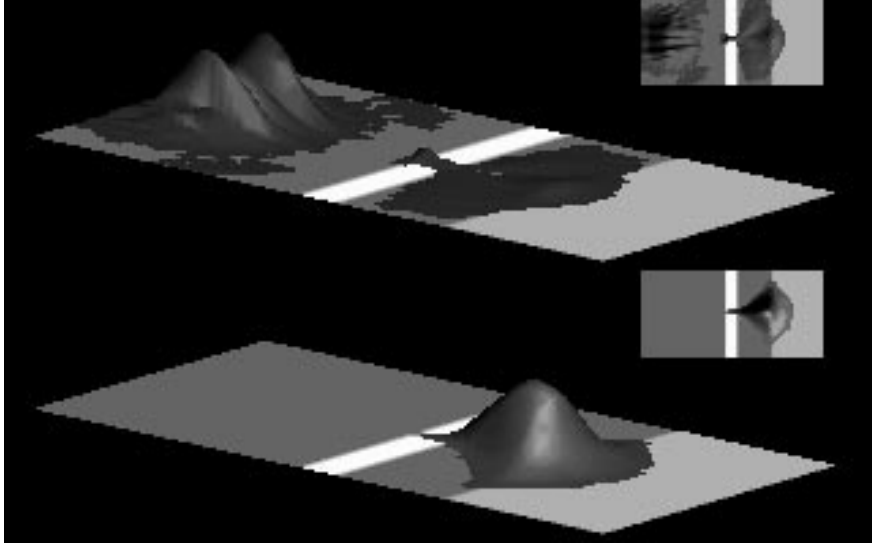
Fig.11. Snapshot of the electron (upper part) and hole (lower part) intensity taken at $t = 160\hbar/E_F$. Normal metal: Dark gray area; Superconductor: Light gray area; Quantum point contact: White structure. Device parameters: $\Delta = 0.067E_F$, $D = 20\lambda_F$, $W = 1.6\lambda_F$, $L = 5\lambda_F$. Intensities left and right of the QPC are scaled differently for visualization purposes.

Simulation of a particular device consists of specifying the potential $V(r)$, the gap $\Delta(r)$ (i.e. the geometry of the device) and the vector potential $A(r)$, setting up the initial state (i.e. an electron wave function $\psi(r,t = 0)$ normalized to one, and $\phi(r,t = 0) = 0$ because there is no hole at $t = 0$) and solving Eq.(49) for times as long as needed to obtain the physically relevant behavior.

The results reported below are for a device of dimensions $340\mu m \times 170\mu m$ with the following characteristics: $E_F = 21\text{meV}$, $m^* = 0.067m_e$, $\Delta = \Delta(r) = 0.067E_F$ (unless explicitly stated otherwise), and $\lambda_F = 335\text{Å}$. For simplicity we will assume that the Fermi-levels of the metal and superconductor are the same. For practical purposes, it is expedient to express energies and distances in units of E_F and λ_F

respectively and we will do so in the sequel. Typically we solve the Bogoliubov-de Gennes equations on a grid of 1024×513 points with mesh size $\delta = \lambda_F/10$, using a time step $\tau = 0.03125\hbar/E_F$ where E_F is the Fermi energy, and 8192 time steps.
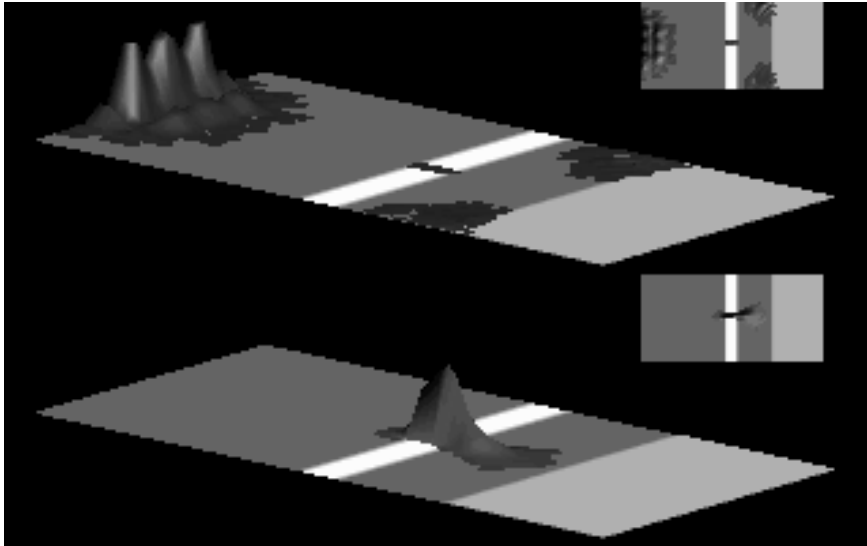
Fig.12. Same as Fig.11 except that $t = 256\hbar/E_F$.

Perfect Andreev scattering, i.e. 100% conversion of electrons into holes, requires that $|E - E_F| \ll \Delta$ where E is the energy of the incoming electron wave, and that $\Delta \ll E_F$.[54,55] In a simulation, the initial wave packet is always confined to a finite region in space and therefore its spread in energy $\sigma_E \neq 0$. Accordingly, (nearly) perfect Andreev scattering demands that $\sigma_E \ll \Delta \ll E_F$, conditions that can only be met by using simulation boxes not smaller than the size indicated above and a wave packet which is as broad as possible. A systematic simulation study for devices without QPC's (not shown) reveals that if the widths of the initial, normalized Gaussian wave packets $\sigma_x = \sigma_y \geq 10\lambda_F$, more than 99% of the electron intensity returns as hole intensity. From an experimental viewpoint this is an acceptable conversion level.

The gaps of conventional superconductors, e.g. Nb compounds, satisfy the condition $\Delta \ll E_F$. In some of the high T$_c$ cuprates $\Delta \approx 0.1E_F$.[59] Therefore, but mainly out of curiosity, it is of interest to solve the Bogoliubov - de Gennes equations for the case where Δ is of the same order of magnitude as E_F. A typical result is shown in Fig.10 where we have taken $\Delta = E_F$. The energy of the incident electron $E = E_F$ and $\sigma_x = \sigma_y = 10\lambda_F$. Part of the electron wave is reflected instead of converted into hole intensity. Only 80% of the incident electron intensity is returning as hole intensity. This effect cannot be accounted for by the standard theoretical treatments[54,55] because the results of these calculations are only valid

in the Andreev limit. Modifying the calculation of ref.55 by taking into account that $\Delta = E_F$ or, in other words, that we are not working in the Andreev limit, we find that about 25% of the electron intensity is reflected at the interface, in fair agreement with the numerically exact result (20%).

Simulation results for several N–S QPC devices with $\Delta = 0.067E_F$ (see Fig.9 for the layout) are shown in Figs.11-14. In all cases the electron wave packet starts from the left of the QPC and is partially reflected by the QPC. The momentum and energy of all initial wave packets $|k| = k_F = 2\pi/\lambda_F$ and $E = E_F$ respectively. The part of the electron wave that emerges from the QPC is spreading out rapidly while it moves towards the N–S interface. The occurrence of diffraction is obviously related to the dimensions of the QPC and is absent in the case of classical ballistic transport.[57] In the superconductor, (part of) the electron wave is converted into a hole wave. The hole wave travels to the left and upon leaving the superconductor, is focussed back into the constriction.
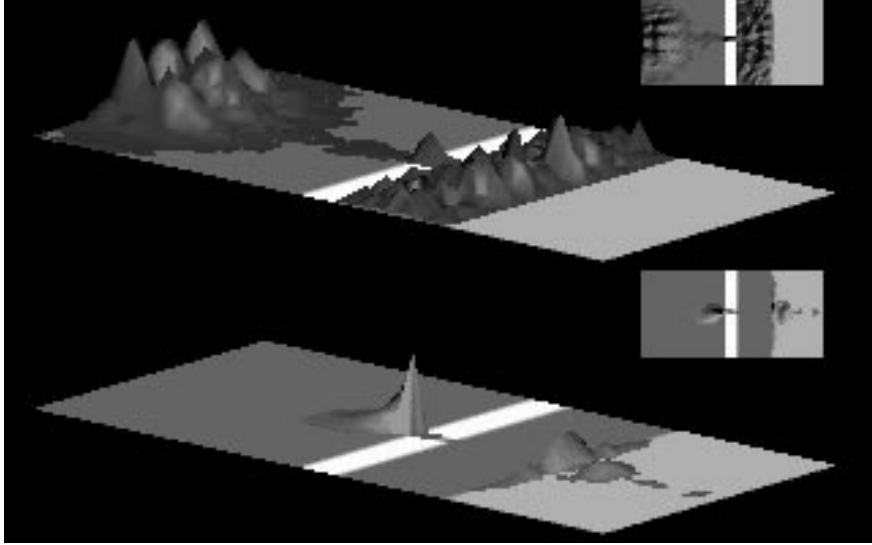
Fig.13. Same as Fig.12 except that at the N–S interface, a tunnel barrier of width $1\lambda_F$ and height $1.2E_F$ is present.

The back-focussing of the hole is most clearly demonstrated in Figs.11,12 where we show the electron and hole intensity at different times t. For visualization purposes, the intensity at the left and right hand side of the exit plane of the QPC are scaled differently. Therefore, Fig.12 might give the impression that there is still a considerable amount of electron (hole) intensity between the QPC and the N–S interface but in fact, the integrated intensity in this part of the device is very small and therefore negligible. The back-focussing effect itself does not depend on the distance D between the QPC and the N–S interface. However, for the device considered here, D is also of the order of λ_F and has an influence on the electron-

hole conversion efficiency.

According to common lore, quantum mechanics forces wave packets to expand not to contract. However, hole waves generated by the Andreev mechanism clearly do contract if the electron wave that caused the hole wave was expanding. This feature is implicit in the Bogoliubov-de Gennes equations (49). From (49), it immediately follows that a hole moves exactly like an electron, except that it moves backward in time. The presence of an external magnetic field breaks the electron-hole symmetry and indeed, our simulations (see Fig.14)) demonstrate that then there is no back-focussing of the hole into the QPC.
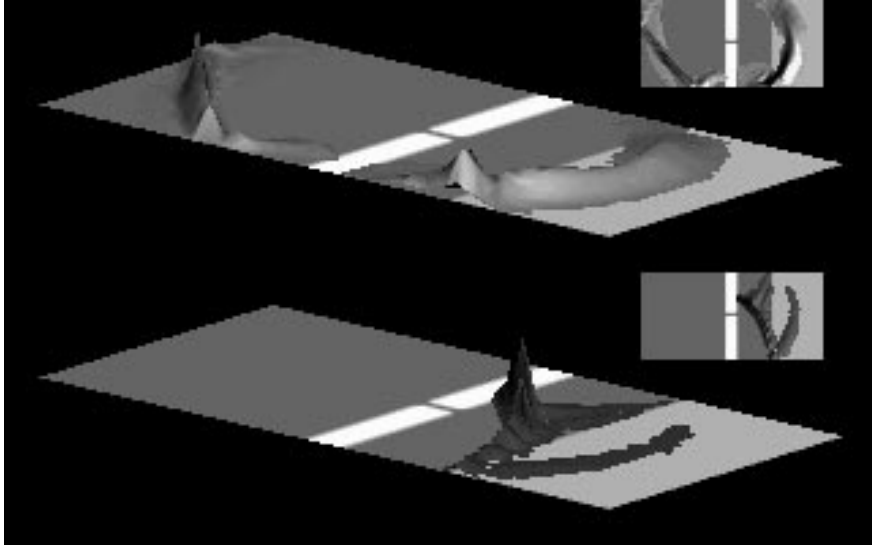
Fig.14. Same as Fig.12 except that an external magnetic field perpendicular to the 2D device penetrates the normal metal. Inside the superconductor, the magnetic field is zero.

Our simulations[24,25] lead to the conclusion that the back-focussing phenomenon itself is extremely robust with respect to changes of devices characteristics, such as the gap Δ, the distance between the QPC and the N–S interface, the width of the QPC, the idealness of the interface, corrugations of the interface, the angle of incidence of the incoming electron wave, the presence of impurities in the region between the QPC and the N–S interface, etc..[24] However, the electron-hole conversion efficiency and therefore also the enhancement of the conductivity does depend on all of the characteristics listed above.[24]

7.3 Aharonov-Bohm and Hanbury-Brown Twiss experiment[60]

Recently Silverman[61,62] proposed and analyzed a thought experiment that combines both the features of the Aharonov-Bohm (AB) and Hanbury-Brown and Twiss (HBT) experiments. The former provides information on the effect of the magnetic field on correlations of two *amplitudes*. The latter on the other hand yields direct information on the correlations of two *intensities*, i.e. of correlations of *four* amplitudes.
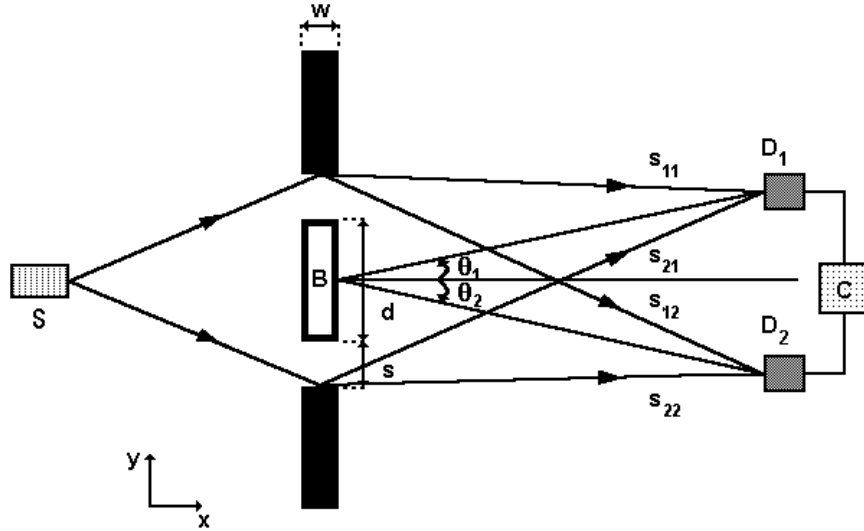
Fig.15. Schematic view of the combined Aharonov-Bohm – Hanbury-Brown-Twiss apparatus. Charged fermions or bosons leave the source S, pass through the double-slit and arrive at detectors D_1 and D_2. The signals of these detectors are multiplied in correlator C. The particles do not experience the magnetic field B enclosed in the double-slit apparatus.

A schematic view of the AB-HBT apparatus is shown in Fig.15. Charged fermions or bosons leave the source S, pass through the double-slit and arrive at detectors D_1 and D_2. In order for the particle statistics to be relevant at all, it is necessary that in the detection area the wave functions of two individual particles overlap. For simplicity, it is assumed that the particles do not interact. The particle statistics may affect the single-particle as well as two-particle interference. The former can be studied by considering the signal of only one of the two detectors. Information on the latter is contained in the cross-correlation of the signals of both detectors. In this section we report some of our results[28] for the AB-HBT thought experiment, as obtained from the numerically exact solution of the time-dependent Schrödinger equation (TDSE).

The algorithm described above can be employed to solve the TDSE for a system of two identical charged but non-interacting particles in an external, inhomogeneous magnetic field, described by the Hamiltonian $\mathcal{H} = \mathcal{H}_1 + \mathcal{H}_2$ where

$$\mathcal{H}_n = \frac{1}{2m} \left(\mathbf{p}_n - e\mathbf{A}(\mathbf{r}_n) \right)^2 + V(\mathbf{r}_n) \quad ; \quad n = 1, 2 \quad , \tag{50}$$

and m is the mass of the particle with charge e, $\mathbf{p}_n = -i\hbar \nabla_n$ is the momentum operator of particle n, and $\mathbf{A}$ represents the vector potential. The potential $V = V(x, y)$ is used to specify the geometry of the two-slit apparatus depicted in Fig.15. A convenient choice for the vector potential is $\mathbf{A} = (A_x(x, y), 0, 0)$ where $A_x(x, y) = -\int_0^y B(x, y) \, dy$. Then the problem is essentially two-dimensional and the motion of the particles may be confined to the x–y plane. The formal solution of the TDSE is given by $|\Phi(m\tau)\rangle = e^{-im\tau\mathcal{H}}|\Phi(t = 0)\rangle = e^{-im\tau\mathcal{H}_1} e^{-im\tau\mathcal{H}_2}|\Phi(t = 0)\rangle$ where $m = 0, 1, \ldots$ counts the number of time-steps τ and use has been made of the fact that the particles do not interact.

In practice we solve the two-particle TDSE subject to the boundary condition that the wave function is zero outside the simulation box, i.e. we assume perfectly reflecting boundaries. The algorithm that we use is an extension of the one described in section 4 and is also accurate to fourth-order in both the spatial and temporal mesh size.[63] Additional technical details can be found elsewehere.[63] Physical properties are calculated from the two-particle amplitude $\Phi(\mathbf{r}, \mathbf{r}', t) = \phi_1(\mathbf{r}, t)\phi_2(\mathbf{r}', t) \pm \phi_2(\mathbf{r}, t)\phi_1(\mathbf{r}', t)$ where $\phi_1(\mathbf{r}, t)$ and $\phi_2(\mathbf{r}, t)$ are the single-particle amplitudes and the plus and minus sign correspond to the case of bosons and fermions respectively.

Let us first reproduce the results of Silverman's analysis.[61,62] Assume that the double-slit apparatus can be designed such that the probability for two identical particles (fermions or bosons) to pass through the same slit can be made negligibly small. The two slits then act as the two sources in the HBT experiment with one modification: Due to the presence of the vector potential the waves can pick up an extra phase shift. According to Silverman,[61,62] it immediately follows that the signal generated by the cross-correlator will *not* show any dependence on the confined magnetic field. The AB shifts for the direct process and the one in which the identical particles have been interchanged mutually cancel. This cancelation is independent of the fact that the particles are fermions or bosons.[64]

The basic assumption of Silverman's analysis is easily incorporated into a computer experiment. The initial two-particle wave function is a properly symmetrized product of single-particle wave functions which, for simplicity, are taken to be Gaussians. Each Gaussian is positioned such that during propagation it effectively "hits" only one slit. The single (top) and correlated (bottom) signals, received by detectors placed far to the right of the slits for $B = 0$ for fermions (l.h.s) as well as for bosons (r.h.s). are shown in Fig.16. For fermions the correlated signal for $\theta_1 = \theta_2$
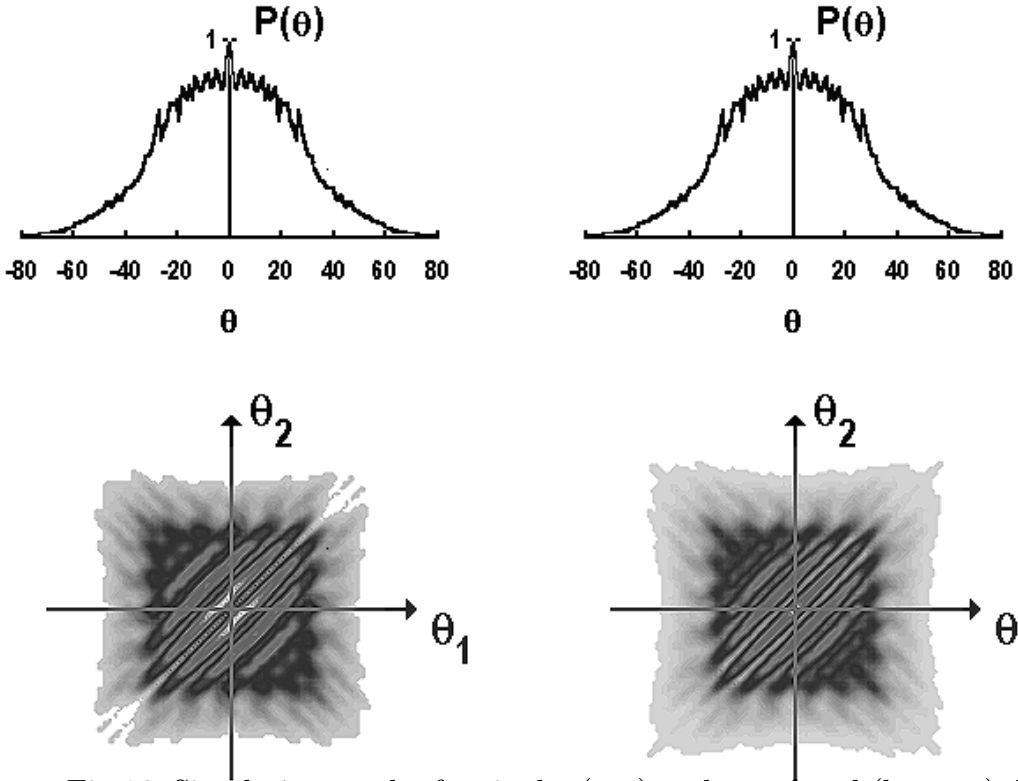
Fig.16. Simulation results for single- (top) and correlated (bottom) detector signal for $B = 0$, obtained from the solution of the TDSE for the initial state as described in the text. Left: Signals generated by fermions. Right: Signals generated by bosons. The corresponding pictures for $B = B_0^{(65)}$ are identical and not shown.

vanishes, as required by the Pauli principle. This feature is hardly visible, due to the resolution we used to generate the pictures but it is present in the raw data.

For bosons as well as for fermions, within four digit accuracy, the corresponding data for $B = B_0$ (or, as a matter of fact, for any B) are identical to those for $B = 0$.[28] Comparison of the cross-correlated intensities (bottom part) clearly lends support to Silverman's conclusion.[61,62] However, it is also clear that the single-detector signals (upper part) do *not* exhibit the features characteristic of the AB effect. Under the conditions envisaged by Silverman, not only is there no AB effect in the cross-correlated signal: There is no AB effect at all.

The absence of the AB effect can be traced back to Silvermans's assumption that the slits can be regarded as sources, thereby eliminating the second, topologically different, alternative for a particle to reach the detector. A different route to arrive at the same conclusion is to invoke gauge invariance to choose the vector potential such that the two particles would never experience a non-zero vector potential.

A full treatment of the thought experiment depicted in Fig.15 requires that *all* possibilities for *both* identical particles are included in the analysis. This is
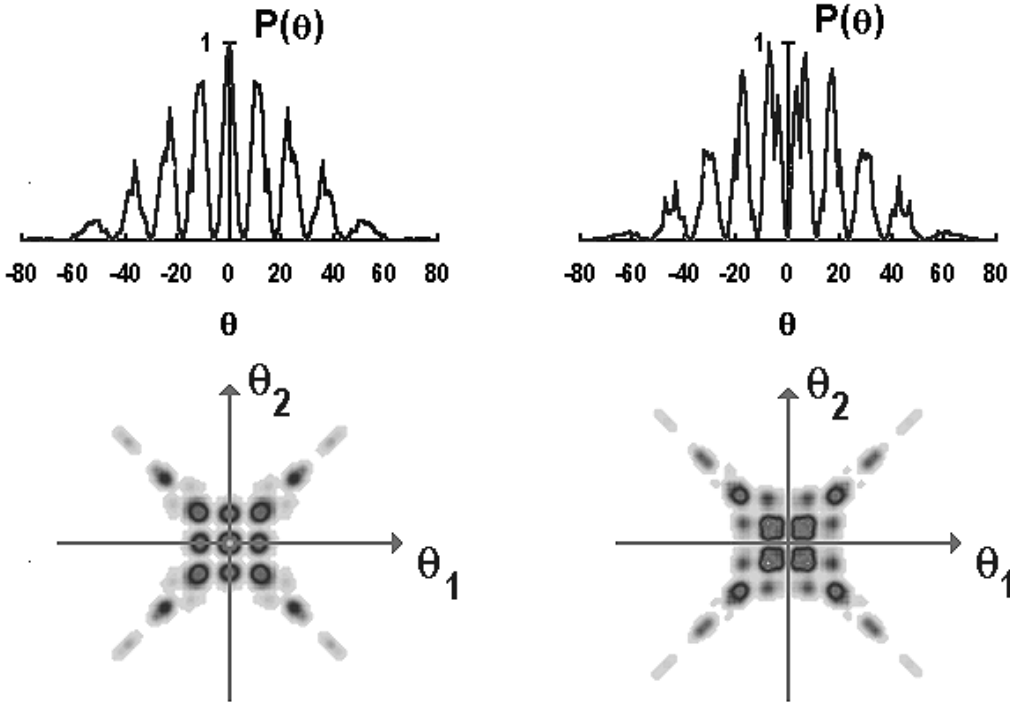
Fig.17. Simulation results for single- (top) and correlated (bottom) detector signal generated by two bosons, as obtained from the solution of the TDSE for the initial state described in the text. Left: $B = 0$. Right: $B = B_0$

easily done in the computer experiment by changing the position and width of the Gaussians used to build the initial wave function of the fermions or bosons such that they both hit the two slits. Some of our results for the case of two bosons are shown in Fig.17. Comparison of the upper parts of Fig.17 provides direct evidence of the presence of the AB effect.

The cross-correlated boson intensities (r.h.s. of the bottom part of Fig.17) clearly exhibit an AB-like effect. The positions of the maxima and minima are interchanged if the magnetic field changes from $B = 0$ to $B = B_0$. We have verified that the shift of these positions is a periodic function of the field B. These results for the case of boson statistics cannot be explained on the basis of Silverman's theory.[61,62]

In general we find that there is only a small quantitative difference between the fermion (l.h.s.) and boson (r.h.s.) single-detector signals: The interference fringes of the fermions are less pronounced than in the case of bosons, another manifestation of the Pauli principle. The differences in the cross-correlated fermion intensities, due to B, are not as clear as in the boson case. Substracting the $B = 0$ from the $B = B_0$ signal and plotting the absolute value of this difference (not shown) clearly shows that also the cross-correlated fermion intensity exhibits features that

are characteristic of the AB effect.[28] The high symmetry in all the correlated signals shown is due to our choice $B = 0, B_0$. The fact that we recover this symmetry in our simulation data provides an extra check on our method. If B is not a multiple of B_0, this high symmetry is lost but the salient features of the signals remain the same. From our numerical experiments, we conclude that in an AB-HBT experiment, an AB shift of the interference pattern will be observed in both the single and two-detector experiments. The AB effect (in both experiments) is more pronounced for bosons than for fermions.

8. Conclusions

The Trotter-Suzuki product-formulae provide the general mathematical setting for constructing algorithms to solve time-dependent quantum problems. These simulation algorithms are powerful tools to investigate various kinds of quantum phenomena.

9. Acknowledgements

10. References

1. S. Washburn, *Nature* **343** (1990) 415.
2. H. van Houten, C.W.J. Beenakker, and B.J. van Wees, *Semiconductors and Semimetals*, edited by M.A. Reed, (New York, Academic 1990).
3. Vu Thien Binh and J. Marien, *Surface Science* **102** (1988) L539.
4. Vu Thien Binh, *J. Microscopy* **152** (1988) 355.
5. M.P. Silverman, W. Strange, and J.C.M. Spence, *Am. J. Phys.* **63** (1995) 800.
6. H. De Raedt, *Comp. Phys. Rep.* **7** (1987) 1.
7. S. Lie and F. Engel, *Theorie der Transformationgruppen*, (Teubner, Leipzig 1888).
8. H. De Raedt, and A. Lagendijk, *Phys. Rep.* **127** (1985) 233.
9. M. Suzuki, *Quantum Monte Carlo Methods*, edited by M. Suzuki, (Solid State Sciences 74, Springer, Berlin, 1986).
10. H. De Raedt and W. von der Linden, *Monte Carlo Methods in Condensed Matter Physics*, edited by K. Binder, (Springer, Berlin, 1992).
11. H.F. Trotter, *Proc. Am. Math. Soc.* **10** (1959) 545.
12. The norm of a matrix X is defined as $\|X\| = M^{-1/2}(\mathbf{Tr}\ X^\dagger X)^{1/2}$.
13. M. Suzuki, *J. Math. Phys.* **601** (1985) 26.
14. H. De Raedt, and B. De Raedt, *Phys. Rev.* **A28** (1983) 3575.
15. M. Suzuki, *J. Math. Phys.* **32** (1991) 400.
16. H. Kobayashi, N. Hatano, and M. Suzuki, *Physica A* **211** (1995) 234.
17. G.D. Smith, *Numerical solution of partial differential equations*, (Clarendon, Oxford 1985).
18. M. Abramowitz and I. Stegun, *Handbook of Mathematical Functions*, (Dover, New York 1964).
19. H. De Raedt, and K. Michielsen , *Computers in Physics* **8** (1994) 600.
20. P. de Vries, H. De Raedt, and A. Lagendijk, *Comp. Phys. Commun.* **75** (1993) 298.
21. N. García, J.J. Sáenz, and H. De Raedt, *J. Phys.: Condens. Matter* **1** (1989) 9931.
22. H. De Raedt, and K. Michielsen, *Nanoscources and Manipulation of Atoms Under High Fields and Temperatures: Applications*, edited by Vu Thien Binh, N. García and K. Dransfeld, (NATO-ASI Series, Kluwer, 1993).
23. K. Michielsen and H. De Raedt, "Electron Focussing", Multimedia Presentation. For more information send e-mail to the author.
24. H. De Raedt, K. Michielsen, and T.M. Klapwijk, *Phys. Rev.* **B50** (1994) 631.
25. H. De Raedt and K. Michielsen, "Andreev Reflection", Multimedia Presentation. For more information send e-mail to the author.

26. H. De Raedt and K. Michielsen, *Comp. in Phys.* **8** (1994) 600.

27. K. Michielsen and H. De Raedt, "Quantum Mechanics", Multimedia Presentation. For more information send e-mail to the author.

28. H. De Raedt and K. Michielsen, *Ann. Physik* **4** (1995) 697.

29. P. de Vries, and H. De Raedt, *Phys. Rev.* **B47** (1993) 7929.

30. S. Miyashita, *J. Phys. Soc. Jpn.* **64** (1995) 3207.

31. D. Garcia–Pablos, N. Garcia, P.A. Serena, and H. De Raedt, "Quantum Dynamical Calculations of the Magnetization Reversal in Clusters of Spin-1/2 Particles: Resonant Coherent Quantum Tunneling" Phys. Rev. B. (in press)..

32. Hiroto Kobayashi, Naomichi Hatano, Akira Terai, and Masuo Suzuki, preprint submitted to Physica A.

33. Based on work carried out in collaboration with N. Garcia, J.J. Saenz, and Vu Thien Binh.

34. D. Gabor, *Proc. Roy. Soc. London* **A454** (1949) 197.

35. D. Gabor, *Proc. Roy. Soc. London* **B64** (1951) 449.

36. A. Tonomura, *Rev. Mod. Phys* **59** (1987) 639.

37. H. Lichte, *Ultramicroscopy* **20** (1986) 293.

38. F.G. Missiroli, G. Pozzi, and U. Valdre, *J. Phys. E* **14** (1981) 649.

39. J.J. Sáenz, N. García, Vu Thien Binh, and H. De Raedt, *Scanning Tunneling Microscopy and Related Methods*, edited by R.J. Behm et al, (Kluwer Academic, Dordrecht, 1990).

40. N.D. Lang, A. Yacobi and Y. Imry, *Phys. Rev. Lett.* **63** (1989) 1499.

41. L.I. Glazman, G.B. Lesovik, D.E. Khmel'nitskii, and R.I. Shekhter, *Sov. Phys. JETP. Lett.* **48** (1988) 238.

42. A. Yacobi, and Y. Imry, *Europhys. Lett.* **11** (1990) 663.

43. A. Yacobi, and Y. Imry, *Phys. Rev. B* **41** (1990) 5341.

44. E. Tekman, S. Ciraci, and A. Baratoff, *Phys. Rev. B* **43** (1991) 7145.

45. K. Michielsen and H. De Raedt, *J. Phys.: Condens. Matt.* **3** (1991) 8247.

46. H. van Houten, C.W.J. Beenakker, and B.J. van Wees, *Semiconductors and Semimetals*, edited by M.A. Reed, (New York, Academic 1990).

47. H. van Houten et al., *Phys. Rev. B* **39** (1989) 8556.

48. H.U. Baranger, and A.D. Stone, *Phys. Rev. Lett.* **63** (1989) 414.

49. H. van Houten, C.W.J. Beenakker, J.G. Williamson, M.E.I. Broekaart, P. van Loosdrecht, B.J. van Wees, J.E. Mooij, C.T. Foxon and J.J. Harris, *Phys. Rev. B* **39** (1989) 8556.

50. U. Sivan, M. Heiblum, C.P. Umbach and H. Shtrikman , *Phys. Rev. B* **41** (1990) 7937.

51. C.W.J. Beenakker and H. van Houten, *Phys. Rev. B* **39** (1989) 10445.

52. M. Born and E. Wolf, *Principles of Optics*, (Pergamon, N.Y. 1959).

53. Based on work carried out in collaboration with K. Michielsen and T.M. Klapwijk, see Ref.24.

54. A.F. Andreev, *Zh. Eksp. Teor. Fiz.* **46**, 1823 (1964) [Sov. Phys. –JETP **19**, 1228 (1964)].
55. G.E. Blonder M. Tinkham, and T.M. Klapwijk, *Phys. Rev. B.* **25** (1982) 4515.
56. H. Takayanagi, and T. Akazaki, *Phys. Rev. B* **52** (1995) R8633.
57. P.A.M. Benistant, A.P. van Gelder, H. van Kempen and P.Wyder, *Phys. Rev. B* **32** (1985) 3351.
58. P.G. de Gennes, *Superconductivity of Metals and Alloys*, (McGraw-Hill, N.Y. 1975).
59. Z.-X. Shen *et al*, *Phys. Rev. Lett.* **70** (1993) 1553.
60. Based on work carried out in collaboration with K. Michielsen, see Ref.26,28.
61. M.P. Silverman, *Am. J. Phys.* **61** (1993) 514.
62. M.P. Silverman, *And Yet It Moves: Strange Systems and Subtle Questions in Physics* , (Cambridge, New York 1993).
63. H. De Raedt, and K. Michielsen, *Computers in Physics* **8** (1994) 600.
64. M.P. Silverman, private communication.
65. B_0 is the magnetic field for which the Aharonov-Bohm shift of the interference pattern is equal to π.